

# UC Berkeley

## UC Berkeley Previously Published Works

### Title

Observationally derived rise in methane surface forcing mediated by water vapour trends

### Permalink

<https://escholarship.org/uc/item/5gc4b6c9>

### Journal

Nature Geoscience, 11(4)

### ISSN

1752-0894

### Authors

Feldman, DR  
Collins, WD  
Biraud, SC  
[et al.](#)

### Publication Date

2018-04-01

### DOI

10.1038/s41561-018-0085-9

Peer reviewed

1 **Title:**

2 Observationally-derived rise in methane surface forcing mediated by water vapour trends

3

4 **Author Information:**

5 D.R. Feldman<sup>1\*</sup>, W.D. Collins<sup>1,2 ‡</sup>, S.C. Biraud<sup>1</sup>, M.D. Risser<sup>1</sup>, D.D. Turner<sup>3</sup>, P.J. Gero<sup>4</sup>, J.

6 Tadic<sup>1</sup>, D. Helmig<sup>5</sup>, S. Xie<sup>6</sup>, E.J. Mlawer<sup>7</sup>, T.R Shippert<sup>8</sup> and M.S. Torn<sup>1,2</sup>

7 **Affiliations:**

8 <sup>1</sup> Lawrence Berkeley National Laboratory, Berkeley, CA, USA.

9 <sup>2</sup> University of California-Berkeley, Berkeley, CA, USA.

10 <sup>3</sup> National Oceanic and Atmospheric Administration Earth Systems Research Laboratory,  
11 Boulder, CO, USA.

12 <sup>4</sup> University of Wisconsin-Madison, Madison, WI, USA.

13 <sup>5</sup> Institute of Arctic and Alpine Research, University of Colorado-Boulder, Boulder, CO, USA.

14 <sup>6</sup> Lawrence Livermore National Laboratory, Livermore, CA, USA.

15 <sup>7</sup> Atmospheric and Environmental Research, Lexington, MA, USA.

16 <sup>8</sup> Pacific Northwest National Laboratory, Richland, WA, USA.

17

18 \*Corresponding Author: 1 Cyclotron Road, MS 74R-316C, Berkeley, CA 94720, USA.

19 [drfeldman@lbl.gov](mailto:drfeldman@lbl.gov)

20 ‡ Denotes co-lead author.

21 **Main Text:**

22 Atmospheric methane (CH<sub>4</sub>) mixing ratios exhibited a plateau between 1995 and 2006 and have  
23 been subsequently increasing. While there are a number of competing explanations for the  
24 temporal evolution of this greenhouse gas, these prominent features in the temporal trajectory of  
25 atmospheric CH<sub>4</sub> are expected to perturb the surface energy balance through radiative forcing,  
26 largely due to CH<sub>4</sub>'s infrared radiative absorption features. However, to date this has been  
27 determined strictly through radiative transfer calculations. Here, we present a quantified  
28 observation of the time-series of clear-sky radiative forcing by CH<sub>4</sub> at the surface from 2002-  
29 2012 at a single site derived from spectroscopic measurements along with line-by-line  
30 calculations using ancillary data. There was no significant trend in CH<sub>4</sub> forcing between 2002  
31 and 2006, but since then, the trend in forcing was  $0.026 \pm 0.09$  (99.7% CI) W/m<sup>2</sup>/yr. The  
32 seasonal-cycle amplitude and secular trends in observed forcing are influenced by a  
33 corresponding seasonal cycle and trend in atmospheric CH<sub>4</sub>. However, we find that we must  
34 account for the overlapping absorption effects of atmospheric water vapour (H<sub>2</sub>O) and CH<sub>4</sub> to  
35 explain the observations fully. Thus, the determination of CH<sub>4</sub> radiative forcing requires accurate  
36 observations of both the spatiotemporal distribution of CH<sub>4</sub> and the vertically resolved trends in  
37 H<sub>2</sub>O.

38

39 **Atmospheric CH<sub>4</sub> and Its Radiative Forcing**

40 The globally-averaged atmospheric mixing ratio of CH<sub>4</sub> has risen since the pre-industrial epoch  
41 from  $722 \pm 25$  ppbv in 1750 to  $1803 \pm 2$  ppbv in 2011<sup>(1)</sup>. However, there is an unresolved debate  
42 regarding the causes of the temporal trajectory of CH<sub>4</sub>, and thus its sources and sinks, over the  
43 last 30 years. The observed plateau in the CH<sub>4</sub> mixing ratio<sup>2</sup> and its end<sup>3</sup> have been attributed to

44 some combination of changes in (1) hydroxyl (OH) radical destruction, (2) tropical wetland  
45 emissions, (3) thawing permafrost and CH<sub>4</sub> hydrates, (4) agriculture, and (5) fossil-fuel  
46 extraction and use, though their relative contributions are ambiguous given existing  
47 observations<sup>4-10</sup>.

48  
49 Rising atmospheric CH<sub>4</sub> mixing ratios are expected to change the distribution of atmospheric  
50 radiative energy, and this is the essential justification for coordinated and prioritized scientific  
51 inquiry regarding atmospheric CH<sub>4</sub>. While substantial resources have been devoted to measuring  
52 increasing atmospheric CH<sub>4</sub><sup>(2,11)</sup> and understanding its anthropogenic contributions<sup>12-14</sup>, the  
53 observational determination of its radiative forcing has, to date, been limited. Satellite  
54 observations have inferred, but not quantified, the radiative forcing associated with rising mixing  
55 ratios of this gas<sup>15,16</sup>. Apart from those efforts, radiative forcing values have been strictly  
56 calculated by radiative transfer models based on information gathered from laboratory  
57 observations. The calculations performed for the IPCC Fifth Assessment report found that CH<sub>4</sub>  
58 has contributed to a stratospherically-adjusted longwave (5-20 μm) radiative forcing at the  
59 tropopause of 0.48±0.05 W/m<sup>2</sup> from the pre-industrial epoch<sup>1</sup>. However, the methods used by  
60 that report were last revised in 1998<sup>(17)</sup>, and recent work has indicated that an upward revision to  
61 the methane radiative forcing formulae and the determination of its global warming potential for  
62 future Assessment Reports is necessary<sup>18</sup>, mostly due to the need to include shortwave effects.

63  
64 The spectroscopy of CH<sub>4</sub>, which is the foundation underlying the radiative forcing calculations,  
65 is an active area of research<sup>19</sup>. This is because CH<sub>4</sub> exhibits a line structure of exceptional  
66 complexity compared to other atmospheric greenhouse gases<sup>20</sup>, and line-by-line calculations and

67 climate model radiation codes must capture this complexity to determine CH<sub>4</sub> radiative forcing.  
68 They do so by using line parameters in spectroscopic databases such as High Resolution  
69 Transmission (HITRAN)<sup>21</sup> and parameterizations of other absorption effects. These databases  
70 are frequently updated, and while the updates have produced only modest changes in CH<sub>4</sub>  
71 infrared forcing<sup>22,23</sup>, the scientific understanding of other potentially significant absorption  
72 effects such as broadening dependencies<sup>24</sup> and H<sub>2</sub>O continuum absorption<sup>18,25</sup> is still advancing.  
73 Alternatively, we can use field observations to establish the sufficiency of the approach by which  
74 CH<sub>4</sub> radiative forcing is solely determined from radiative transfer calculations.

75

76 The specialized, long-duration suite of observations collected at the U.S. Department of Energy  
77 Atmospheric Radiation Measurement (ARM) Program<sup>26</sup> at the Southern Great Plains (SGP) site  
78 (36° 36' 18" N, 97° 29' 6" W) provide a unique opportunity to observe greenhouse gases and  
79 their forcing, as indicated by the first observation of the increase in the greenhouse effect from  
80 rising atmospheric concentrations of CO<sub>2</sub><sup>(27)</sup>.

81

82 The time-series of weekly CH<sub>4</sub> surface flask measurements from SGP shows a high variability in  
83 CH<sub>4</sub> at SGP, with boundary layer excursions sometimes exceeding 2300 ppbv (Figure 1). As  
84 with other locations of high-precision atmospheric CH<sub>4</sub> measurements, the time-series of CH<sub>4</sub>  
85 mixing ratios shows fine-scale temporal variability. At SGP, some of the excursions may be due  
86 to local hydrocarbon recovery, based on the correlation between CH<sub>4</sub> and ethane mixing  
87 ratios<sup>28,29</sup> (see Methods). Meanwhile, an analysis of these instantaneous CH<sub>4</sub> observations (see  
88 Methods) shows (1) no significant trend in atmospheric CH<sub>4</sub> before 2007, (2) a break-point in

89 2007, and (3) that CH<sub>4</sub> mixing ratios have been rising at a rate of 7.5±4.4 (95% CI) ppbv/yr since  
90 then.

91  
92 While other studies have observed trends in the surface energy balance with broadband  
93 radiometry<sup>30,31</sup>, broadband observations are inadequate for attributing changes in that balance to  
94 changes in atmospheric composition of specific gas species. Therefore, we use a long time-series  
95 of clear-sky downwelling spectral infrared radiance observations to determine if changes in  
96 atmospheric CH<sub>4</sub> mixing ratios have a discernible effect on the surface energy balance. We focus  
97 here on longwave clear-sky flux changes since they are predicted to be the most sensitive  
98 longwave radiative flux signal associated with rising greenhouse gases<sup>32</sup> and since detailed all-  
99 sky forcing calculations of the study site indicate that most of the forcing arises under clear-sky  
100 conditions (see Methods).

101

### 102 **CH<sub>4</sub> Radiative Forcing Dependencies**

103 Figure 2(a) shows, through radiative transfer calculations, that the infrared emission by CH<sub>4</sub> that  
104 contributes to its longwave surface radiative forcing occurs predominantly between 1200 and  
105 1350 cm<sup>-1</sup>. However, as the radiative transfer calculations in Figure 2(b) show, the determination  
106 of CH<sub>4</sub> forcing is complicated by a significant H<sub>2</sub>O and N<sub>2</sub>O dependence of the downwelling  
107 flux in the CH<sub>4</sub> absorption band, arising from the overlap of spectral absorption features of H<sub>2</sub>O  
108 and N<sub>2</sub>O with those of CH<sub>4</sub>. The downwelling flux is also highly temperature-dependent both  
109 due to Planck function and absorption line temperature dependence. Fortunately, the surface  
110 mixing ratios for N<sub>2</sub>O are highly correlated with its mixing ratios throughout the column (Figure  
111 2(c)), so the radiative effects of N<sub>2</sub>O can be estimated using a near-surface measurement of its

112 mixing ratio. Radiosonde data at the ARM SGP site were used to control for variability in the  
113 atmospheric thermodynamic state<sup>33</sup>. Airborne measurements indicate that boundary-layer and  
114 free tropospheric fluctuations in CH<sub>4</sub> mixing ratios are not highly correlated at subseasonal time-  
115 scales. Therefore, surface observations of CH<sub>4</sub> mixing ratio alone are insufficient for calculating  
116 CH<sub>4</sub> forcing at the time-scales of our analysis.

117  
118 CH<sub>4</sub> surface radiative forcing was derived from 11 years' of infrared spectroscopic observations  
119 made by the Atmospheric Emitted Radiance Interferometer (AERI)<sup>34</sup>. The forcing was  
120 determined by differencing AERI measurements with counterfactual line-by-line calculations<sup>27</sup>  
121 where the thermodynamic state is prescribed by concurrent radiosonde observations<sup>33</sup>, but the  
122 calculation used a pre-industrial CH<sub>4</sub> mixing ratio (see Methods). Detailed data quality control  
123 and averaging methods were used to account for the effects of uncertainties in temperature, H<sub>2</sub>O,  
124 and N<sub>2</sub>O, and the effect of instrumental noise, respectively (see Methods). The minimum  
125 temporal resolution of the observations used here was 6 hours (see Methods). From this process  
126 chain, we observe the direct, unadjusted, instantaneous radiative forcing at the surface, which,  
127 while not biased by the effects of thermodynamics (see Methods), is still affected by them.  
128 Ideally, measurements would be made under prescribed thermodynamic conditions, but we have  
129 no means of controlling for these conditions in the field.

130  
131 The mean spectral residuals were prominent only in the spectral region of CH<sub>4</sub> absorption (see  
132 Methods) and therefore exclude the possibility that uncertainties in the atmospheric state and  
133 instrument calibration were substantially affecting the results. Top-down validation of our  
134 forcing estimates, based on *in situ* observations by simultaneous aircraft overflights<sup>35</sup>, indicates

135 that we can observe instantaneous CH<sub>4</sub> forcing to within 0.14 W/m<sup>2</sup> (see Methods). Sensitivity  
136 tests (see Methods) reveal that the transient plumes of boundary layer methane would lead to an  
137 instantaneous surface radiative forcing signal of 0.05 W/m<sup>2</sup>, so our analysis is unable to discern  
138 the transient contribution of anthropogenic activity to observed forcing. However, suprasedasonal  
139 time-series features of atmospheric CH<sub>4</sub> mixing ratios, which do contain contributions from  
140 human activity<sup>4-10</sup>, are readily discernible in the observed radiative forcing.

141

### 142 **Observationally-Derived Forcing Time-Series and Influence of Thermodynamics**

143 Irrespective of the source of the atmospheric CH<sub>4</sub>, we derive a time-series of CH<sub>4</sub> surface  
144 longwave radiative forcing from observations that exhibits several prominent features (Figure 3).  
145 During the multi-year atmospheric CH<sub>4</sub> plateau, the trend in this forcing did not differ  
146 significantly from zero (p>0.1). The time-series exhibited a significant change around 2007 at  
147 the end of the plateau (p<0.0001). From then onwards, the trend differed from zero at  
148 0.026±0.006 W/m<sup>2</sup>/yr (99.7% CI). During the 11-year record, there was a large seasonal cycle,  
149 with an amplitude of at least 0.2 W/m<sup>2</sup>.

150

151 During the time period of the atmospheric CH<sub>4</sub> plateau, it is expected that there would not be  
152 significant trends in surface radiative forcing from CH<sub>4</sub>, and this was confirmed by observations.  
153 However, the amplitude of the seasonal cycle in surface forcing throughout the time-series and  
154 the forcing trend since 2006 cannot be fully explained by the atmospheric CH<sub>4</sub> mixing ratio at  
155 SGP. The amplitude of the seasonal cycle in CH<sub>4</sub> dry atmospheric mixing ratio is 51.2±10.1  
156 (99.7% CI) ppbv, and, based on the mean water vapor profile during the observational period at  
157 the SGP, the seasonal cycle amplitude would be 0.012±0.002 (99.7% CI) W/m<sup>2</sup>, significantly



158 smaller than the observed amplitude of  $0.25 \pm 0.01$  (99.7% CI)  $\text{W/m}^2$ . The observed trend in  $\text{CH}_4$   
159 since 2007 is  $7.5 \pm 6.6$  (99.7% CI)  $\text{ppbv/yr}$  which, again based on the mean water vapor profile  
160 during the observational period at the SGP, would yield a trend of  $0.002 \pm 0.0009$  (99.7% CI)  
161  $\text{W/m}^2/\text{yr}$ , significantly smaller than the observed trend of  $0.026 \pm 0.006$  (99.7% CI)  $\text{W/m}^2/\text{yr}$ .  
162 However, analyzing the time-series in isolation from thermodynamics is highly idealized, can  
163 yield varying results depending on the choice of thermodynamic conditions, and is inconsistent  
164 with actual conditions in the field. Nevertheless, this discrepancy must be resolved.

165

166 We can exclude several potential explanations for these findings; for example, the contributions  
167 of observational error and analysis error would produce spectral residuals outside of the  $\text{CH}_4$   
168 absorption band and time-series statistics that are inconsistent with our findings. Possible  
169 contributions from other radiatively-active trace gases in the  $\text{CH}_4$  absorption band between 1200  
170 and  $1350 \text{ cm}^{-1}$  can also be excluded (see Methods).

171

172 Rather, we find that when we perform a multivariate signal decomposition analysis of the  
173 deseasonalized time-series of  $\text{CH}_4$  forcing constructed over the entire time-series using a  
174 nonlinear predictor based solely on  $\text{CH}_4$  concentrations, we can explain roughly 80% of the  
175 variation in observed forcing ( $R^2=0.793$ ), implying that at least 20.7% of the variance is related  
176 to other factors (see Methods).

177

178 Rather, we find that the contribution of trends and variability in water vapour to those in  $\text{CH}_4$   
179 surface forcing are significant. Even though the residual spectra indicate that we are not  
180 imprecisely specifying atmospheric temperature and moisture,  $\text{CH}_4$  forcing is nonetheless

181 dependent on atmospheric state. The primary reason for this water vapour dependence is that  
182 mid-IR CH<sub>4</sub> absorption occurs at the edge of a strong ν<sub>2</sub> H<sub>2</sub>O absorption band. Therefore,  
183 elevated H<sub>2</sub>O mixing ratios saturate the CH<sub>4</sub> band<sup>36</sup> and reduce the latter molecule's radiative  
184 forcing, as shown in Figures 4(d). Indeed, we performed a model-only computation based on  
185 observed thermodynamics and CH<sub>4</sub> mixing ratios and obtain a trend of 0.020±0.009 (99.7% CI)  
186 W/m<sup>2</sup>/yr, which is not distinguishable (p>0.05) from the observationally-derived trend.  
187 Additionally, this effect is largely insensitive to the observed mid-tropospheric temperature  
188 changes, as shown in Figure 4(c).

189  
190 For the seasonal cycle, we find that the water vapour seasonal cycle of 7.7±0.03 g/kg helps  
191 explain the seasonal cycle in observed CH<sub>4</sub> surface forcing. For trends, we note that a long-term  
192 decreasing trend in moisture availability in the central US has been observed<sup>37</sup>. This was also  
193 observed in a 14-year analysis of AERI clear-sky radiances<sup>38</sup>. At SGP, an analysis of radiosondes  
194 coincidental to the CH<sub>4</sub> forcing observations is consistent with that finding and yields negative  
195 trends in atmospheric moisture in the lowest 1 km, as shown in Figure 4(b). While no significant  
196 change point in the vertically-resolved time-series is observed, column water decreased by 30%  
197 since the end of the CH<sub>4</sub> plateau. This negative trend over the entire time-series and especially  
198 since the end of the CH<sub>4</sub> plateau will tend to enhance CH<sub>4</sub> forcing, and provides the opportunity  
199 to analyze the alternating effects of CH<sub>4</sub> and H<sub>2</sub>O on the observed forcing. Figure 5 shows that  
200 the observed forcing trends in CH<sub>4</sub> forcing could be reproduced only when we include nonlinear  
201 predictors that include both CH<sub>4</sub> concentration and observed thermodynamic trends (R<sup>2</sup>=0.997,  
202 see Methods). Specifically, trends in CH<sub>4</sub> surface flask measurements and trends in height-  
203 resolved temporal profiles of temperature and humidity can be used to predict both plateau and

204 post-plateau surface radiative forcing trends after all variables are decomposed into frequency  
205 noise (5a), a seasonal component (5b), and deseasonalized trends (5c), yielding a normally-  
206 distributed residual signal (5d). The result is that the first temperature and moisture principal  
207 components, covering the lower 5 km of the atmosphere, explain nearly all of the signal's  
208 variance (5e and 5f).

209

### 210 **Broader Implications**

211 This study presents the first observational derivation and quantification of the effect of time-  
212 varying CH<sub>4</sub> on the clear-sky surface energy balance, with a large seasonal cycle amplitude of  
213 0.25 W/m<sup>2</sup> and a significant difference in forcing trends at SGP during and after the CH<sub>4</sub> plateau.  
214 The decadal-averaged trend in surface forcing was larger for CO<sub>2</sub> than CH<sub>4</sub> at this site, but the  
215 perturbation of the surface energy balance from rising CH<sub>4</sub> mixing ratios since the end of the  
216 plateau was similar to the effect from rising CO<sub>2</sub> (0.02±0.007 W/m<sup>2</sup>/yr) at the site. Though this  
217 difference was not statistically significant (p>0.3), it suggests that, since the end of the plateau,  
218 the role of rising CH<sub>4</sub> in perturbing the surface energy balance can be highly dependent on local  
219 water vapour trends<sup>39-42</sup>. At SGP, CH<sub>4</sub> surface forcing trends are not necessarily inferior to that  
220 of CO<sub>2</sub>, even though forcing at tropopause by CO<sub>2</sub> is much more than CH<sub>4</sub><sup>(1)</sup>.

221

222 These observations show a long-term trend in CH<sub>4</sub> surface radiative forcing, with variance from  
223 a function of rising CH<sub>4</sub> mixing ratios and the non-negligible contribution that depends on the  
224 vertical distribution of water vapour. This finding is related to tropopausal radiative forcing,  
225 which figures prominently in the scientific discussion of how rising CH<sub>4</sub> impacts average  
226 tropospheric temperatures<sup>1</sup>, but spatial patterns in upper tropospheric moisture<sup>43</sup> mediate forcing

227 at the tropopause, while surface humidity more strongly affects surface forcing. For this  
228 investigation, we find that trends in surface forcing from greenhouse gases are convolved with  
229 the details of how the thermodynamic state of the atmosphere is evolving, and the local  
230 thermodynamic conditions must be taken into account. Since local temperature and humidity  
231 trends that are distinct from those at SGP exist at other sites, the relative contributions of  
232 thermodynamics and mixing ratio changes to the forcing may also differ. Observed trends in  
233 surface humidity have not been spatially or temporally uniform, nor have they been monotonic.  
234 The magnitude of the globally-averaged land-surface humidity trend varies on decadal time-  
235 scales while also exhibiting trends that are spatially variable over land and that show strong land-  
236 ocean contrast<sup>39-42</sup>. Therefore, the direct impact of greenhouse gases on the surface energy  
237 balance cannot be predicted in isolation from thermodynamics. Nevertheless, as we have shown,  
238 CH<sub>4</sub> surface radiative forcing trends can be derived from measurements and quantified  
239 spectroscopically.

240 **References:**

- 241 1. Myhre, G., *et al.* *Climate Change 2013: The Physical Science Basis. Contribution of*  
242 *Working Group I to the Fifth Assessment Report of the Intergovernmental Panel on*  
243 *Climate Change Ch. 8* (Cambridge University Press, Cambridge, United Kingdom and  
244 New York, NY, USA, 2013).
- 245 2. Dlugokencky, E.J., Nisbet, E.G., Fisher, R. & Lowry, D. Global atmospheric methane:  
246 budget, changes and dangers. *Philos. Trans. R. Soc. London Ser. A.* **369**, 2058-2072  
247 (2011).
- 248 3. Nisbet, E.G., Dlugokencky, E.J. & Bousquet, P. Methane on the rise—again. *Science*  
249 **343**, 493-495 (2014).
- 250 4. Kirschke, S., *et al.* Three decades of global methane sources and sinks. *Nat. Geosci.* **6**,  
251 813-823 (2013).
- 252 5. Aydin, M., *et al.* Recent decreases in fossil-fuel emissions of ethane and methane derived  
253 from firm air. *Nature* **476**, 198-201 (2011).
- 254 6. Kai, F.M., Tyler, S.C., Randerson, J.T. & Blake, D.R. Reduced methane growth rate  
255 explained by decreased Northern Hemisphere microbial sources. *Nature* **476**, 194-197  
256 (2011).
- 257 7. Schaefer, H., *et al.* A 21<sup>st</sup> century shift from fossil-fuel to biogenic methane emissions  
258 indicated by <sup>13</sup>CH<sub>4</sub>. *Science* **352**, 80-84 (2016).
- 259 8. Prather, M.J. & Holmes, C.D. Overexplaining or underexplaining methane's role in  
260 climate change. *Proc. Natl. Acad. Sci. USA.* **114**, 5324-5326 (2017).
- 261 9. Rigby M, *et al.* Role of atmospheric oxidation in recent methane growth. *Proc Natl.*  
262 *Acad. Sci. USA.* **114**, 5373–5377 (2017).

- 263 10. Turner, A.J., Frankenberg, C., Wennberg, P.O. & Jacob, D.J. Ambiguity in the causes for  
264 decadal trends in atmospheric methane and hydroxyl. *Proc Natl. Acad. Sci. USA*. **114**,  
265 5367–5372 (2017).
- 266 11. Bergamaschi, P., *et al.* Atmospheric CH<sub>4</sub> in the first decade of the 21st century: Inverse  
267 modeling analysis using SCIAMACHY satellite retrievals and NOAA surface  
268 measurements. *J. Geophys. Res.* **118**, 7350–7369 (2013).
- 269 12. Turner, A.J., *et al.* A large increase in U.S. methane emissions over the past decade  
270 inferred from satellite data and surface observations. *Geophys. Res. Lett.* **43**, 2218–2224  
271 (2016).
- 272 13. Miller, S.M., *et al.* Anthropogenic emissions of methane in the United States. *Proc. Natl.*  
273 *Acad. Sci. USA*. **110**, 20018–20022 (2013).
- 274 14. Brandt, A.R., *et al.* Methane leaks from North American natural gas systems. *Science*.  
275 **343**, 733–735 (2014).
- 276 15. Harries, J.E., Brindley, H.E., Sagoo, P.J. & Bantges, R.J. Increases in greenhouse gas  
277 forcing inferred from outgoing longwave spectra of the Earth in 1970 and 1997. *Nature*  
278 **410**, 355–357 (2001).
- 279 16. Griggs, J.A. & Harries, J.E. Comparison of spectrally resolved outgoing longwave  
280 radiation over the tropical Pacific between 1970 and 2003 using IRIS, IMG, and AIRS. *J.*  
281 *Climate* **20**, 3982–4001 (2007).
- 282 17. Myhre, G., Highwood, E.J., Shine, K.P. & Stordal, F. New estimates of radiative forcing  
283 due to well mixed greenhouse gases. *Geophys. Res. Lett.* **25**, 2715–2718 (1998).

- 284 18. Etminan, M., Myhre, G., Highwood, E.J. & Shine, K.P. Radiative forcing of carbon  
285 dioxide, methane, and nitrous oxide: A significant revision of the methane radiative  
286 forcing. *Geophys. Res. Lett.* **43**, 12614-12623 (2016).
- 287 19. Brown, L.R., *et al.* Methane line parameters in the HITRAN2012 database. *J. Quant.*  
288 *Spectrosc. Rad. Trans.* **130**, 201-219 (2013).
- 289 20. Goody, R.M. & Yung, Y.L. *Atmospheric Radiation: Theoretical Basis Ch. 3* (Oxford  
290 Univ. Press, New York, 1989).
- 291 21. Rothman, L.S., *et al.* The HITRAN2012 molecular spectroscopic database. *J. Quant.*  
292 *Spectrosc. Rad. Trans.* **130**, 4-50 (2013).
- 293 22. Kratz, D.P. The sensitivity of radiative transfer calculations to the changes in the  
294 HITRAN database from 1982 to 2004. *J. Quant. Spectrosc. Rad. Trans.* **109**, 1060-1080,  
295 (2008).
- 296 23. Lu, P., Zhang, H. & Jing, X. The effects of different HITRAN versions on calculated  
297 long-wave radiation and uncertainty evaluation. *Acta Meteor. Sin.* **26**, 389-398 (2012).
- 298 24. Delahaye, T., *et al.* Measurements of H<sub>2</sub>O broadening coefficients of infrared methane  
299 lines. *J. Quant. Spectrosc. Rad. Trans.* **173**, 40-48 (2016).
- 300 25. Mlawer, E. J., *et al.* Development and recent evaluation of the MT\_CKD model of  
301 continuum absorption. *Phil. Trans. Roy. Soc. A.* **370**, 1-37 (2012).
- 302 26. Turner, D.D. & Ellingson, R.G. *The Atmospheric Radiation Measurement Program: The*  
303 *First 20 Years*, (Amer. Meteor. Soc., Boston, 2016).
- 304 27. Feldman, D.R., *et al.* Observational determination of surface radiative forcing by CO<sub>2</sub>  
305 from 2000 to 2010. *Nature* **519**, 339-343 (2015).

- 306 28. Helmig, D., *et al.* Reversal of global atmospheric ethane and propane trends largely due  
307 to US oil and natural gas production. *Nature Geo.* **9**, 490-495 (2016).
- 308 29. Hausmann, P., Sussmann, R., & Smale, D. Contribution of oil and natural gas production  
309 to renewed increase in atmospheric methane (2007-2014): top-down estimate from ethane  
310 and methane column observations. *Atmos. Chem. Phys.* **16**, 3227-3244 (2016).
- 311 30. Wild, M., *et al.* The global energy balance from a surface perspective. *Clim. Dynam.* **40**,  
312 3107-3134 (2013).
- 313 31. Wang, K. & Liang, S. Global atmospheric downward longwave radiation over land  
314 surface under all-sky conditions from 1973 to 2008. *J. Geophys. Res.* **114**, D19101,  
315 (2009).
- 316 32. Stephens, G.L., *et al.* An update on Earth's energy balance in light of the latest global  
317 observations. *Nature Geosci.* **5**, 691-696 (2012).
- 318 33. Xie, S., *et al.* Clouds and more: ARM Climate Modeling Best Estimate Data. *Bull. Amer.*  
319 *Meteor. Soc.* **91**, 31-20 (2010).
- 320 34. Knuteson, R.O., *et al.* Atmospheric Emitted Radiance Interferometer. Part I: Instrument  
321 design. *J. Atmos. Ocean. Technol.* **21**, 1763-1776 (2004).
- 322 35. Biraud, S.C., *et al.* A multi-year record of airborne CO<sub>2</sub> observations in the US Southern  
323 Great Plains. *Atmos. Meas. Tech.* **6**, 751-763 (2013).
- 324 36. Huang, Y., Tan, X. & Xia, Y. Inhomogeneous radiative forcing of homogeneous  
325 greenhouse gases. *J. Geophys. Res.* **121**, 2780-2789 (2016).
- 326 37. Jung, M., *et al.* Recent decline in the global land evapotranspiration trend due to limited  
327 moisture supply. *Nature* **467**, 951-954 (2010).



- 328 38. Gero, P.J. & Turner, D.D. Long-term trends in downwelling spectral infrared radiance  
329 over the U.S. Southern Great Plains. *J. Climate*. **24**, 4831-4843 (2011).
- 330 39. Willett, K.M., *et al.* HadISDH: an updateable land surface specific humidity product for  
331 climate monitoring. *Clim. Past*. **9**, 657-677 (2013).
- 332 40. Dai, A. Recent climatology, variability, and trends in global surface humidity. *J. Climate*.  
333 **19**, 3589-3606 (2006).
- 334 41. Berry, D.I. & Kent, E.C. A new air-sea interaction gridded dataset from ICOADS with  
335 uncertainty estimates. *Bull. Amer. Meteor. Soc.* **90**, 645-656 (2009).
- 336 42. Simmons, A.J., Willett, K.M., Jones, P.D., Thorne, P.W. & Dee, D.P. Low frequency  
337 variations in surface atmospheric humidity, temperature, and precipitation: Inferences  
338 from reanalyses and monthly gridded observational data sets. *J. Geophys. Res.* **115**,  
339 D01110 (2010).
- 340 43. Wentz, F.J., Ricciardulli, L., Hilburn, K. & Mears, C. How much more rain will global  
341 warming bring? *Science*, **317**, 233–235 (2007).
- 342 44. Anderson, G.P., *et al.* AFGL atmospheric constituent profiles (0–120 km). AFGL-  
343 TR\_86-0110 (1989).

344 **Acknowledgements:** This material is based upon work supported by the Director, Office of  
345 Science, Office of Biological and Environmental Research of the U.S. Department of Energy  
346 (DOE) under Contract No. DE-AC02-05CH11231 as part of their Atmospheric System Research  
347 (ASR) Program and the Atmospheric Radiation Measurement (ARM) Program and Terrestrial  
348 Ecosystem Sciences Programs (TES), and the ARM Aerial Facility (AAF), and used resources of  
349 the National Energy Research Scientific Computing Center (NERSC) under the same contract.  
350 Work at LLNL was performed under the auspices of the U.S. DOE by Lawrence Livermore  
351 National Laboratory under contract No. DE-AC52-07NA27344. M. Alvarado, K. Cady-Pereira,  
352 L. Riihimaki, I. Simpson and P. Novelli also contributed. NOAA GMD provided flask CH<sub>4</sub>,  
353 C<sub>2</sub>H<sub>6</sub>, and N<sub>2</sub>O data.

354

355 **Author Contributions:** D.R.F. led the research, performed all calculations, and wrote the  
356 manuscript; W.D.C. proposed the study concept, provided research guidance, and conceived  
357 methods for isolating the CH<sub>4</sub> signal; S.C.B. provided CH<sub>4</sub> and N<sub>2</sub>O data and associated support;  
358 M.D.R. provided the statistical analysis; D.D.T. provided guidance on AERI instrument  
359 performance and research focus; P.J.G. helped interpret AERI data; J.T. analyzed  
360 thermodynamic contributions to the observed forcing. D.H. provided C<sub>2</sub>H<sub>6</sub> data and associated  
361 support; S.X. provided ARMBE data and associated support; E.J.M. and T.R.S. provided clear-  
362 sky error analysis; M.S.T. provided research feedback and guidance and served as P.I. of the  
363 grant supporting this research. All authors discussed the results and commented on the  
364 manuscript.

365

366 **Competing financial interests:** The authors declare no competing financial interests.

367 **Figure Captions:**

368

369 **Figure 1:** Recent evolution of atmospheric methane at the surface study site.

370 Time-series of the annual distribution of surface flask measurements of CH<sub>4</sub> at DOE ARM SGP

371 site. Box-whisker plots show the mean (+), median (line), the box bounding the 25- and 75-

372 percentile and the whiskers set at the 0.1- and 99.9-percentile for weekly flask measurements

373 from a given year. Least-squares linear trend analyses are included for selected time periods

374 before and after 2007 (vertical dashed line). The 2007 change-point was determined from weekly

375 time-series data (see Methods).

376

377 **Figure 2:** Factors affecting CH<sub>4</sub> longwave surface instantaneous radiative forcing.

378 (a) Change in spectral flux for a 1 ppbv perturbation in CH<sub>4</sub> for a 1 km layer in a Mid-Latitude

379 Summer (MLS) profile<sup>44</sup>. (b) Vertical sensitivity of downwelling surface flux in CH<sub>4</sub> absorption

380 band to 1 km perturbations in temperature, H<sub>2</sub>O, N<sub>2</sub>O, and CH<sub>4</sub> derived from LBLRTM radiative

381 transfer calculations with the MLS profile (c) Box-whisker diagrams of the vertical distribution

382 of CH<sub>4</sub> and N<sub>2</sub>O, with inset of associated correlation coefficient in mixing ratio between the

383 surface and a given height, from aircraft observations<sup>35</sup> at SGP from flights 2002-2012. Box

384 spans 25<sup>th</sup> to 75<sup>th</sup> percentile, whisker spans 5<sup>th</sup> to 95<sup>th</sup> percentile of observations.

385

386 **Figure 3:** CH<sub>4</sub> longwave surface radiative forcing time-series.

387 Time-series (black), 2 $\sigma$  instantaneous uncertainty in CH<sub>4</sub> surface longwave radiative forcing

388 (gray; see Methods) and trends with 3 $\sigma$  uncertainty (red; *ibid.*) at DOE ARM SGP.

389

390 **Figure 4:** Thermodynamic dependence of CH<sub>4</sub> surface forcing.

391 (a) Vertically-resolved slope of ARMBE temperature measurements with the 99.7% confidence-  
392 interval. (a) Same as (b) but for trends in the logarithm of specific humidity. (c) Surface radiative  
393 forcing vs. tropospheric-averaged CH<sub>4</sub> as a function of temperature perturbations from 8 to 16.5  
394 km from a mid-latitude summer atmosphere<sup>44</sup>. The change in mid-level temperature over the  
395 observed time-period was  $0.4 \pm 0.2$  °K (99.7% CI) and is indicated on the plot (d) Same as (c) but  
396 for humidity perturbations in g/kg from 0 to 1 km. The change in boundary-layer water vapour  
397 over the observed time-period was  $-1.5 \pm 1.0$  g/kg (99.7% CI) and is indicated on the plot.

398

399 **Figure 5:** Forcing time-series decomposition and reconstruction from predictors

400 (a) Time-series of CH<sub>4</sub> forcing signal noise removed by Random forest with 100 weak learners.  
401 (b) Seasonal forcing signal. (c) Deseasonalized forcing signal. (d) Histogram of observed vs  
402 decomposed and reconstructed forcing. (e) First component of Principal Component Analysis  
403 (PCA) of temperature predictors (f) First component of PCA for humidity predictors. See  
404 Methods for details.

405 **Methods:**

406 CH<sub>4</sub> surface radiative forcing was determined by differencing measured spectra from the AERI  
407 instrument<sup>45</sup>, subject to quality control (see below), with radiative transfer calculations using 512  
408 levels of temperature and humidity from radiosondes profiles as processed by the ARM Best  
409 Estimates (ARMBE)<sup>33,46</sup>, ozone from the Modern-Era Retrospective Analysis for Research and  
410 Applications (MERRA)<sup>47</sup>, CO<sub>2</sub> profiles from the nearest spatiotemporal grid point from  
411 CarbonTracker-CO2 2013<sup>(48)</sup>, monthly-averaged N<sub>2</sub>O mixing ratios from the Mauna Loa  
412 Observatory (MLO)<sup>49</sup>, and pre-industrial (722 ppbv) CH<sub>4</sub> mixing ratios. This counterfactual  
413 calculation, designed to simulate the spectrally-resolved radiance field at the Earth's surface, had  
414 CH<sub>4</sub> mixing ratios remained at annually-averaged pre-industrial levels<sup>27</sup>. The counterfactual was  
415 created using the Line-by-Line Radiative Transfer Model (LBLRTM) version 12.2, using the  
416 AER line parameter database version 3.1<sup>(50)</sup> based on HITRAN 2008<sup>(51)</sup> with updated line-  
417 mixing<sup>52</sup> and the MT\_CKD\_2.5.2 H<sub>2</sub>O continuum absorption model<sup>25</sup>. Limb-brightening factors,  
418 converting both observations and calculations from radiance to flux, were calculated with three-  
419 point Gaussian quadrature over zenith angle<sup>53</sup>. Supplementary Information Figure 1 shows a  
420 schematic of this process chain.

421

422 **Data Quality Control**

423 AERI spectra were recorded every 8 minutes from the instrument's initial deployment to April  
424 2004 (at SGP). Subsequently, spectra were recorded every 30 seconds, with only minor outages,  
425 in order to provide higher temporal-resolution data for cloud studies<sup>54</sup>. This analysis only  
426 considered data starting in 2002 because the ARMBE data are derived from Vaisala RS-80  
427 profiles prior to 2002 and that instrument suffered a known dry bias<sup>55,56</sup>. The end of the analysis

428 period was the start of 2013, which was chosen because the AERI instrument at SGP  
429 experienced a failure and was replaced in mid-2013. The analysis could be extended beyond  
430 early 2013 but would have to address complications from changing instrumentation<sup>57</sup>.  
431  
432 Only the subset of spectra recorded within 2 hours of a radiosonde launch were utilized. With 4  
433 daily launches, each measurement is separated by a minimum of 6 hours and spans 4 hours.  
434 Based on the radiosonde profile, a radiance spectrum was calculated using LBLRTM with 512  
435 levels of temperature and relative humidity from the ARMBE product<sup>33</sup>. All AERI spectra  
436 recorded within 2 hours of the radiosonde launch were rank-ordered by the root-mean-squared  
437 brightness temperature of the residual spectrum of the difference between the measurement and  
438 the LBLRTM calculation between 600 and 980  $\text{cm}^{-1}$ . This range was chosen to be sensitive to  
439 thermodynamic conditions but insensitive to  $\text{CH}_4$  or ozone, where the latter is strongly  
440 influenced by MERRA biases<sup>58</sup>. The rank-ordered spectra were averaged sequentially together  
441 (i.e., the first two spectra were averaged, then the first three spectra were averaged, etc.) and the  
442 RMS of the residual between that average and the LBLRTM calculation was recalculated. The  
443 sequential average of the spectra that produced the minimum RMS of the residual relative to the  
444 radiosonde-based LBLRTM calculation was used as the AERI spectral measurement for  
445 subsequent analysis. The rationale for this approach is to average as many spectra together as  
446 possible to minimize random measurement error, but to avoid biasing the spectra by averaging  
447 observations during which clouds were present or where the thermodynamic conditions had  
448 changed relative to the radiosonde.

449

450 Since the determination of CH<sub>4</sub> surface forcing is so dependent on an accurate specification of  
451 the atmospheric thermodynamic profile, we apply additional tests of the sequentially averaged  
452 spectra against the counterfactual calculations to remove cases where the thermodynamic or  
453 condensate profiles differ substantially between the observation and the counterfactual. First, we  
454 evaluate the RMS of the residual between the AERI spectral measurement and the LBLRTM  
455 calculation between 790 and 810 cm<sup>-1</sup> (hereafter referred to as the 800 cm<sup>-1</sup> channel), because  
456 this region is sensitive to atmospheric temperature, humidity, and condensates (see  
457 Supplementary Information Figures 2(a) and 2(b)). These plots show the slope and correlation  
458 coefficient of the least-squares relationship between the radiative flux sensitivity to moisture and  
459 temperature perturbations for a given channel outside the CH<sub>4</sub> absorption feature (1200-1350 cm<sup>-1</sup>)  
460 and the average radiative flux sensitivity to moisture and temperature perturbations within the  
461 CH<sub>4</sub> absorption feature. The least-squares relationship is derived from six model atmospheres,  
462 which span a wide range of terrestrial thermodynamic conditions<sup>44</sup>. The upper panels of Figures  
463 (2a) and (2b) show that fluxes in the spectral region between 790 and 810 cm<sup>-1</sup> are more  
464 sensitive to perturbations in temperature and moisture than fluxes in the CH<sub>4</sub> absorption band.  
465 The lower panels show that perturbations in temperature and moisture produce flux perturbations  
466 in the 790-810 cm<sup>-1</sup> spectral region and the CH<sub>4</sub> absorption band that are highly correlated.

467

468 We also utilize the RMS of the residual between 705 and 709 cm<sup>-1</sup> (hereafter referred to as the  
469 707 cm<sup>-1</sup> channel), which is sensitive to the atmospheric boundary layer temperature.

470 Supplementary Information Figure 2(c) shows the gain and correlation coefficient for the  
471 relationship between the variance of a spectral channel outside the CH<sub>4</sub> absorption feature and  
472 the variance of the spectral channel within the CH<sub>4</sub> absorption feature, where both are calculated

473 with the measurements and calculations used in the aircraft validation cases (see below). This  
474 figure shows that the  $707\text{ cm}^{-1}$  variance is highly correlated with the variance within the  $\text{CH}_4$   
475 band across a range data wherein the  $800\text{ cm}^{-1}$  tolerance criterion is satisfied below 5 K. A gain  
476 of greater than unity, indicating high sensitivity to boundary-layer temperature perturbations, is  
477 also shown at  $707\text{ cm}^{-1}$  for the same  $800\text{ cm}^{-1}$  tolerance criterion.

478

479 Only spectral residuals with an RMS residual spectrum brightness temperature at  $800\text{ cm}^{-1}$  of  
480 less than 3 K and a standard deviation at  $707\text{ cm}^{-1}$  less than 0.3 K (after averaging) are  
481 considered for subsequent analysis. See Supplemental Information for the rationale for these  
482 threshold choices.

483

484 Supplementary Information Figure 4 shows the average residual spectrum featuring a large  
485 deviation from zero where  $\text{CH}_4$  has a prominent absorption due to the use of a pre-industrial  $\text{CH}_4$   
486 mixing ratio for the counterfactual calculation and deviations equivalent to less than 1 K in  
487 temperature, 10 ppmv  $\text{CO}_2$ , 5% percent  $\text{H}_2\text{O}$ , and 10%  $\text{N}_2\text{O}$ . The exception lies in the  $9.6\text{ }\mu\text{m}$   
488 ozone absorption band between  $980$  and  $1080\text{ cm}^{-1}$ , indicating a systematic overestimation of  
489 column ozone from the MERRA data products at SGP<sup>58</sup>. The lack of prominent spectral  
490 structures outside the  $\text{CH}_4$  and  $\text{O}_3$  bands excludes other possible explanations including cloud  
491 contamination, water vapour or temperature bias, or instrument calibration, all of which produce  
492 spectral residuals with characteristic features not solely in the  $\text{CH}_4$  absorption band.

493

494 **Time-Series Decomposition**



495 We tested the hypothesis that the cause for the observed trend in radiative forcing could be  
496 contained within a set of predictors including height-resolved trends in water vapour, height-  
497 resolved trends in temperature, and ground level methane concentration measured by flasks. If  
498 we cannot use these predictors to reproduce the observed forcing, we can infer that there are  
499 other contributing factors to the forcing that we have not considered. For the reconstruction of  
500 this time-series, we used a two-step decomposition of all predictors using a widely utilized and  
501 flexible approach that avoids overfitting<sup>59</sup>. First, we isolated the component of the unfiltered  
502 signal that cannot be described as white noise or outlier data using a calibrated Random forest  
503 with 100 weak learners<sup>59</sup>. A calibrated Random forest was used to reproduce the signal at the  
504 desired points in time, and the difference between the reproduced and actual signal was filtered  
505 out. Second, the remaining noise and cyclical components of the signal were removed using  
506 moving average filter with a 12-month window<sup>60</sup>. The size of the moving-average filter window  
507 was selected because the signal exhibited clear annual seasonal variations.

508

509 With this approach, we created a set of isolated trends for 1025 predictors (512 each for  
510 temperature and humidity and 1 for flask CH<sub>4</sub> observations). To make the problem less  
511 computationally expensive, and given the extreme level of redundancy in vertically-resolved  
512 temperature and water-vapour predictors, we applied principal component analysis (PCA) for the  
513 reduction of dimensionality<sup>61</sup>. The fraction of variance explain by the first 5 principal  
514 components (out of 512) was found to be >99.99% for both temperature and humidity,  
515 confirming the high-degree of redundancy in the predictors. With 5 PCs for temperature, 5 for  
516 humidity, and 1 for methane concentration, we created a reduced set of 11 predictors to describe  
517 the CH<sub>4</sub> radiative forcing trend. An ensemble of five back-propagation neural networks was then

518 trained to reproduce the trend component of the CH<sub>4</sub> radiative forcing<sup>62</sup>. To avoid over-fitting,  
519 the training and reproduction of the radiative forcing was done in leave-one-out fashion, such  
520 that the radiative forcing value to be reconstructed from the predictors is withheld from the  
521 training set. Instead, ensemble neural networks are trained using the remaining data points, and  
522 then the network is used to reproduce the withheld data point. The procedure was repeated  
523 sequentially for all data points.

524

525 With this approach, the correlation coefficient between the observed trends in the entire CH<sub>4</sub>  
526 surface forcing time-series and the neural-network prediction where all 11 predictors are used is  
527 0.9983 ( $R^2=0.997$ ). Where only the CH<sub>4</sub> flask data is used as a predictor to train the network, the  
528 correlation coefficient is 0.8907 ( $R^2=0.793$ ). More specifically, we can explain ~80% of the  
529 variance in radiative forcing using custom-designed non-linear predictor. However, we should  
530 note that our signal is obtained from the difference between an observation and calculation,  
531 which is not best possible non-linear predictor, so the amount of variance that can be explained  
532 using only CH<sub>4</sub> concentrations is necessarily less than 80%. Rather, our results produce an  
533 estimate of the minimum of the fraction of variance that cannot be explained using the  
534 predictor(s) of interest. They also show that information from temperature and humidity, and not  
535 just CH<sub>4</sub> flask concentration data, is needed to describe the observed trend in CH<sub>4</sub> surface  
536 radiative forcing.

537

538 **Statistical Analysis Methods**

539 The statistical analysis of the time-series seeks to determine whether and when a change point  
540 occurred in the measured CH<sub>4</sub> surface radiative forcing, as well as the linear (temporal) trends  
541 and their significance. The following describes the methods used to perform this analysis.

542

543 Define  $y_t$  as the CH<sub>4</sub> forcing for the SGP site at time  $t = 1, \dots, T$ . Our statistical model is:

544

$$545 \quad y_t = b_0 + b_1 t + b_2 X_t(t - t_0) + a_j + e_t + v_t, \quad (1)$$

546

547 where  $\{b_k\}$  are unknown regression coefficients,  $\{a_j\}$  represent (unknown) monthly effects,  $e_t$  are  
548 independent and identically distributed (iid)  $N(0, s^2)$  with  $s^2$  unknown ( $N(a, b)$  denotes a  
549 univariate Gaussian random variable with mean  $a$  and variance  $b$ ), and  $v_t$  iid  $N(0, w^2)$  with  $w^2$   
550 known (also,  $e_t$  and  $v_t$  are independent). The model (1) contains two error processes: first,  $e_t$   
551 represents error in the model specification and therefore  $s^2$  is estimated; second,  $v_t$  represents  
552 error introduced by the measurement process on  $y_t$  and therefore  $w^2$  will be considered fixed (see  
553 Statistical Analysis Results). The variable  $X_t$  is defined to be 0 if  $t \leq t_0$  and 1 if  $t > t_0$ , and the  
554 change point must fall between fixed bounds  $T_U < t_0 < T_L$ . Therefore, for  $t \leq t_0$ , the monthly-  
555 adjusted trend in expected CH<sub>4</sub> forcing has slope  $b_1$ ; for  $t > t_0$ , the trend has slope  $b_1 + b_2$ .

556

557 The unknown parameters in (1) and the change point can be estimated using a common  
558 (Frequentist) statistical technique called maximum likelihood (ML)<sup>63</sup>, which also yields  
559 confidence intervals for the regression coefficients<sup>64</sup>. Given the setup in (1), we can determine  
560 the significance of the change point  $t_0$  by way of model selection: the full model (1) can be vs.

561  $H_1: b_2 \neq 0$ ). A test of  $H_0$  can be done using a standard full vs. reduced model  $F$ -test for nested  
562 models<sup>64</sup>.

563

564 The Frequentist analysis described above ignores any uncertainty in estimating the change point,  
565 and the model is not well suited to assess this uncertainty (outside of asymptotic evaluations)<sup>65</sup>.

566 Alternatively, a Bayesian approach can be used to determine the significance of the change point  
567 while accounting for its uncertainty (again using model comparison). Bayesian models that  
568 mirror the full (1) and reduced (2) models can be set up using noninformative prior distributions  
569 and estimated using Markov Chain Monte Carlo (MCMC) methods<sup>66</sup>. MCMC output can be used  
570 to compare the full and reduced models using Bayes factors<sup>67</sup>.

571

## 572 **Statistical Analysis Results**

573 The aforementioned models were fit for many different data sets from the SGP site. This data set  
574 was created by using values of the  $800 \text{ cm}^{-1}$  brightness temperature (BT) residual threshold  
575 parameter ranging from 0.1 to 10 (see Data Quality Control). However, if the data set for a  
576 particular threshold value had fewer than 50 observations, the analysis was not conducted. The  
577 upper and lower limits of the change point were fixed to  $T_L = 2004$  and  $T_U = 2010$ ; any potential  
578 change points near the beginning or end of the time series are not of interest. The seasonal cycle  
579 of  $\text{CH}_4$  due to hydroxyl radical destruction is captured via the monthly effects  $\{a_j\}$ ; for  
580 comparison, all models were fit and results presented both with and without the monthly effects.

581

582 For the ML models, plots of the estimated change point, significance of the change point, and  
583 estimates of the slope parameters (with 99.7% confidence intervals) from both before and after

584 the change point are provided in Supplementary Information Figures 5 and 6. Results from the  
585 Bayesian models were approximately identical to the ML models and are omitted. Based on the  
586 similarity of results, the main text used the more familiar Frequentist results including the  
587 monthly adjustment.

588

589 Supplementary Information Table 1 numerically summarizes the results of the statistical analysis  
590 used in the main text where the  $800\text{ cm}^{-1}$  BT threshold is 3 K.

591

### 592 **Controlling for N<sub>2</sub>O**

593 The methods used to determine CH<sub>4</sub> surface radiative forcing can be biased by N<sub>2</sub>O. Figure 2(b)  
594 shows this due to the substantial amount of overlap in spectral radiance changes from  
595 perturbations from N<sub>2</sub>O and CH<sub>4</sub>. However, the vertical profiles of N<sub>2</sub>O collected by the ARM-  
596 ACME missions<sup>35</sup> at SGP show that N<sub>2</sub>O mixing ratios at altitude are highly vertically-correlated  
597 with the surface (see insets of Figure 2(c)) and vary by less than 1 ppbv seasonally.

598

599 Moreover, these differ very little from measurements at MLO. The error incurred in CH<sub>4</sub> forcing  
600 from utilizing monthly-averaged MLO N<sub>2</sub>O observations instead of in situ ARM-ACME N<sub>2</sub>O  
601 observations was maximized at 1.2% of the CH<sub>4</sub> forcing.

602

603 N<sub>2</sub>O can still bias CH<sub>4</sub> forcing because it is emitted after precipitation following the nearby fresh  
604 application of nitrogen-based fertilizer<sup>68</sup>, causing >5 ppbv deviations from the background N<sub>2</sub>O  
605 mixing ratio. NEXRAD data<sup>69</sup> were used to screen data to remove those observations for which  
606 precipitation had occurred in the previous 24 hours.

607

### 608 **Instantaneous Error**

609 There are several sources of error in the determination of the surface forcing from the AERI  
610 measurements. They include (1) spectroscopic error in LBLRTM; (2) AERI measurement error;  
611 (3) error in the temperature, water vapour, CO<sub>2</sub>, or O<sub>3</sub> inputs to LBLRTM inputs; and (4) a  
612 contribution of unknown aerosol or cloud condensates to the AERI observations. While the error  
613 contributions from (1) are outside of the scope of this analysis, we can perform a top-down  
614 estimate of errors from (2) through (4) with AERI measurements and LBLRTM calculations  
615 using inputs from simultaneous aircraft profiles.

616

617 Surface radiative forcing time series from the aircraft data were derived from differencing AERI  
618 observations with counterfactual calculations. These were compared with the surface radiative  
619 forcing time series computed by differencing an LBLRTM calculation with the aircraft-observed  
620 profile of CH<sub>4</sub> and N<sub>2</sub>O and the counterfactual calculation.

621

622 Supplementary Information Figure 8 show the standard deviation of AERI-observed and aircraft-  
623 derived surface radiative forcing. Figure 3 shows that an abscissa value of 3 K corresponds to an  
624 ordinate value of 0.14 W/m<sup>2</sup>, which is thus our estimate of the 1- $\sigma$  instantaneous error in  
625 radiative forcing.

626

### 627 **Ethane Data Analysis**

628 Supplementary Information Figures 9(a) and 9(b) show time-series analyses of ethane (C<sub>2</sub>H<sub>6</sub>)  
629 flask data. Non-Methane Hydrocarbon (NMHC) flask data from SGP were first filtered for

630 outliers; values that deviated more than  $2\text{-}\sigma$  from a running median were excluded from trend  
631 analyses. Filtered data were then uploaded to the NOAA server for filtering and trends were  
632 determined using the method of Thoning et al.<sup>70</sup>

633

### 634 **Clear-Sky Bias**

635 We evaluate the potential for clear-sky bias in the determination of  $\text{CH}_4$  surface radiative  
636 forcing. We estimate this bias by recalculating the Broadband Heating Rate Profile (BBHRP)<sup>71</sup>  
637 profiles at SGP for 2010 based on pre-industrial  $\text{CH}_4$  mixing ratios and comparing those to the  
638 original BBHRP profiles, containing time-varying  $\text{CH}_4$  derived from the nearest grid box from  
639 CarbonTracker- $\text{CH}_4$ <sup>(72)</sup>. We then subset the data identified as clear-sky in the Radiatively  
640 Important Parameters Best Estimate (RIPBE) product<sup>73</sup>.

641

642 We find that most of the forcing is in the clear-sky but that the all-sky surface forcing is  $0.065$   
643  $\text{W}/\text{m}^2$ , or 33%, less than the clear-sky forcing. This finding is expected because of non-negligible  
644 overlap between broadband cloud absorption and  $\text{CH}_4$  absorption, thereby masking  $\text{CH}_4$  forcing.  
645 This cloud-masking may vary year-to-year. Currently, the independent estimates of cloud  
646 vertical profiles produce residual spectra with signatures of clouds, so the effect of  $\text{CH}_4$  cannot  
647 be isolated under all-sky conditions.

648

### 649 **Non-Methane Contributions to Observed Signal**

650 The possibility that condensates or non-methane gaseous atmospheric constituents are  
651 contributing to the observed  $\text{CH}_4$  surface forcing must be considered. The contribution of  
652 condensates can be excluded because they produce broadband signals that are not observed in the

653 residual spectra. We can also address the non-methane gaseous constituent question by  
654 determining the effects of perturbations in the atmospheric concentrations of 32 additional  
655 species with spectroscopy tabulated in HITRAN<sup>21</sup>, and found their contributions to be at least 5  
656 orders of magnitude smaller than CH<sub>4</sub>.

657

### 658 **Flasks-Based Observations**

659 At the SGP site, a pair of 2.5 liters glass flasks is collected on a weekly basis from the top of the  
660 central facility 60m tower. Flask collection started in April 2002 and is currently ongoing. The  
661 collection of a pair of flasks allows basic quality assessment and control. These observations are  
662 part of the NOAA's Global Greenhouse Gases Reference Network (REF)<sup>74</sup>. Flasks are collected  
663 in the afternoon, when the planetary boundary layer is well-developed and observations are  
664 representative of a large area. Aircraft profiles of CH<sub>4</sub> and N<sub>2</sub>O were recorded on approximately  
665 a bi-monthly basis from 2002 until the present (see Supplementary Information Figures 7(a) and  
666 7(b)).

667

668 Ground-based and aircraft-based flasks are analyzed after they are collected at NOAA/ESRL by  
669 gas chromatography, and measurements are reported against WMO CH<sub>4</sub>-X2004 and N<sub>2</sub>O  
670 X2006A scales. Flask-based observations are shown to have uncertainties of less than 1.2 ppbv  
671 for CH<sub>4</sub> and 0.4 ppbv for N<sub>2</sub>O.

672

### 673 **Aircraft Validation**

674 Aircraft profiles of CH<sub>4</sub> and N<sub>2</sub>O above the SGP site were recorded on approximately a weekly  
675 basis with flask observations from 2002 until the present. Prior to 2006, the flasks were



676 collected only at 0.6 and 3.6 km, but since then, flasks were collected at 12 elevations between  
677 0.5 km and 5.5 km above sea level (see Supplementary Information Figures 7(a) and 7(b)).

678

### 679 **Single-Site Analysis**

680 The analysis presented here focused on the SGP site. Several other ARM sites exist, including  
681 the North Slope of Alaska (NSA) site, and AERI data from that site was analyzed for previous  
682 work<sup>27</sup>. For the CH<sub>4</sub> analysis, however, differences in the instrumental noise in the AERI  
683 instrument at NSA greatly complicated the analysis there. In particular, the Extended—Range  
684 AERI at NSA has an expanded spectral range compared to the AERI at SGP, leading to higher  
685 instrumental (random) noise over 1200-1350 cm<sup>-1</sup> spanning the dominant CH<sub>4</sub> absorption  
686 feature<sup>75</sup>.

687

### 688 **Residual Brightness Temperature Threshold Rationale**

689 The rationale for choosing a threshold of 3 K brightness temperature is based on balancing the  
690 number of data points with error in the CH<sub>4</sub> surface forcing determination, both of which will  
691 increase with increasing threshold values. Another related factor for the determination of an  
692 appropriate threshold is the importance of observations throughout the year. The 3 K threshold  
693 enables a determination of the seasonal cycle in surface forcing at the SGP site and summertime  
694 multi-year trends at the NSA site. Supplementary Information Figure 3 shows the relationships  
695 between the 800 cm<sup>-1</sup> brightness temperature residual threshold and the number of data points.

696

### 697 **Data Availability**

698 The ARM data and radiative transfer codes used in this analysis are freely available to download  
699 from <http://www.archive.arm.gov/discovery/> and <http://rtweb.aer.com>, respectively. The  
700 following are URLs from which input data can be downloaded:

701 MERRA: <http://goldsmr3.sci.gsfc.nasa.gov/.opendap/MERRA/MAI3CPASM.5.2.0/contents.html>

702 CarbonTracker-CO2: <ftp://aftp.cmdl.noaa.gov/products/carbontracker/co2/molefractions/>

703 CarbonTracker-CH4: <ftp://aftp.cmdl.noaa.gov/products/carbontracker/ch4/molefractions/>

704 NOAA CH<sub>4</sub> data: <http://ds.data.jma.go.jp/gmd/wdcgg/pub/data/current/ch4/>

705 NOAA N<sub>2</sub>O data:

706 [ftp://aftp.cmdl.noaa.gov/data/hats/n2o/insituGCs/CATS/daily/mlo\\_N2O\\_Day.dat](ftp://aftp.cmdl.noaa.gov/data/hats/n2o/insituGCs/CATS/daily/mlo_N2O_Day.dat)

707 NOAA C<sub>2</sub>H<sub>6</sub> data: <http://ds.data.jma.go.jp/gmd/wdcgg/pub/data/current/vocs/ethane/event/>

708 Reprints and permissions information is available at <http://www.nature.com/reprints>

709

## 710 **Code Availability**

711 The computer code developed for this research was written in Matlab and will be made available  
712 upon request.

713 **References:**

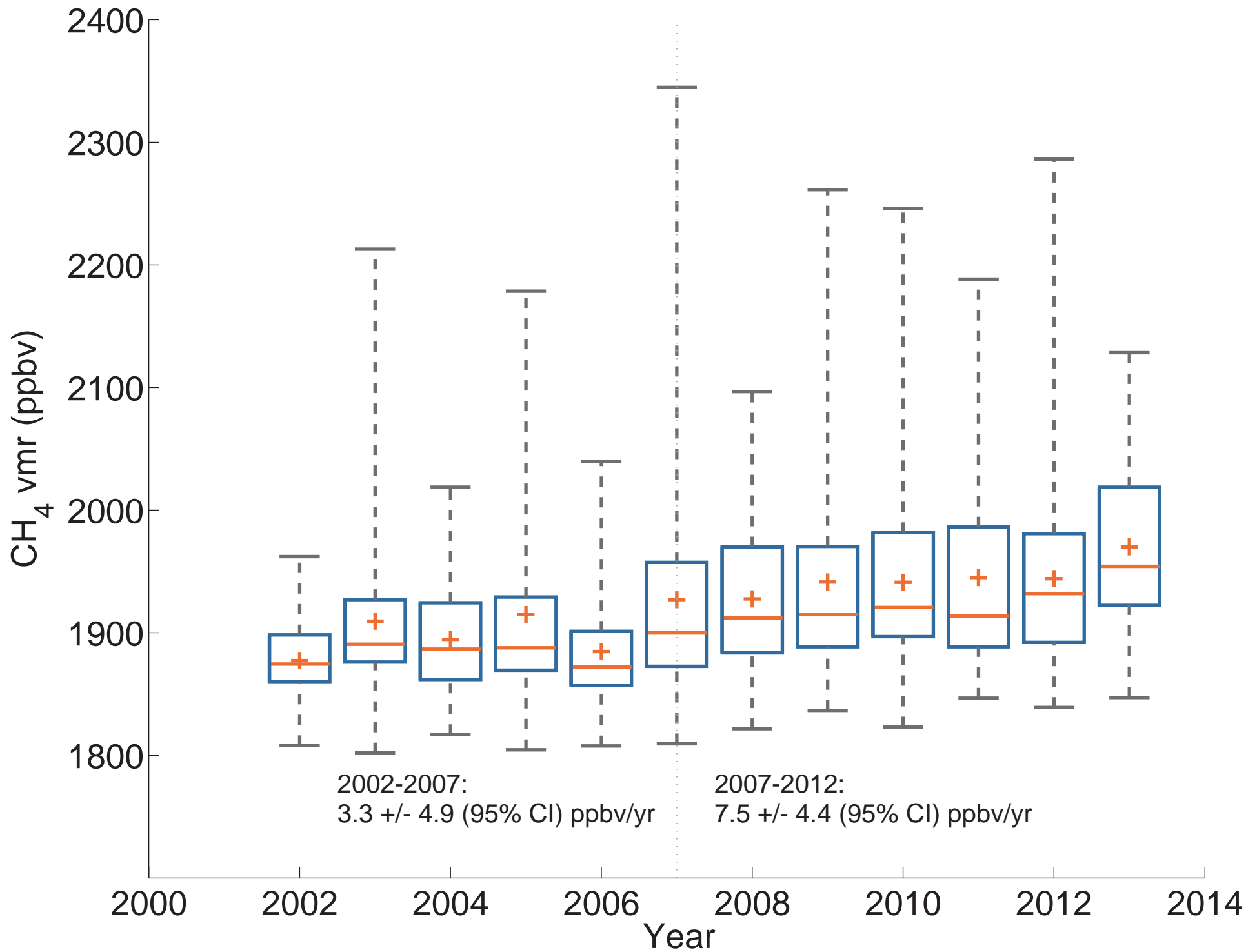
- 714 45. Atmospheric Radiation Measurement (ARM) Climate Research  
715 Facility. 1994, updated **hourly**. Atmospheric Emitted Radiance Interferometer  
716 (AERICH1). **2000-01-01 to 2015-06-01, 36.605 N 97.485 W: Southern Great Plains**  
717 **(SGP) Central Facility, Lamont, OK (C1)**. Compiled by J. Gero, B. Ermold, A.  
718 Koontz, K. Gaustad, D. Hackel and R. Garcia. Atmospheric Radiation Measurement  
719 (ARM) Climate Research Facility Data Archive: Oak Ridge, Tennessee, USA. Data set  
720 accessed **2015-06-01** at <http://dx.doi.org/10.5439/1025143>.
- 721 46. Atmospheric Radiation Measurement (ARM) Climate Research  
722 Facility. 1994, updated **yearly**. ARM Best Estimate Data Products  
723 (ARMBEATM). **2012-01-01 to 2012-12-31, 36.605 N 97.485 W: Southern Great**  
724 **Plains (SGP) Central Facility, Lamont, OK (C1)**. Compiled by X. Chen and S.  
725 Xie. Atmospheric Radiation Measurement (ARM) Climate Research Facility Data  
726 Archive: Oak Ridge, Tennessee, USA. Data set accessed **2015-06-**  
727 **01** at <http://dx.doi.org/10.5439/1039931>.
- 728 47. Rienecker, M.M., *et al.* MERRA: NASA's Modern-Era Retrospective Analysis for  
729 Research and Applications. *J. Climate* **24**, 3624–3648 (2011).
- 730 48. Peters, W., *et al.* An atmospheric perspective on North American carbon dioxide  
731 exchange: CarbonTracker. *Proc. Natl. Acad. Sci. USA*. **104**, 18925-18930 (2007).
- 732 49. Nitrous Oxide data from the NOAA/ESRL halocarbons in situ program. Calibration  
733 scale used: NOAA 2006A More information about the calibration scale can be found at:  
734 <http://www.esrl.noaa.gov/gmd/ccl/>

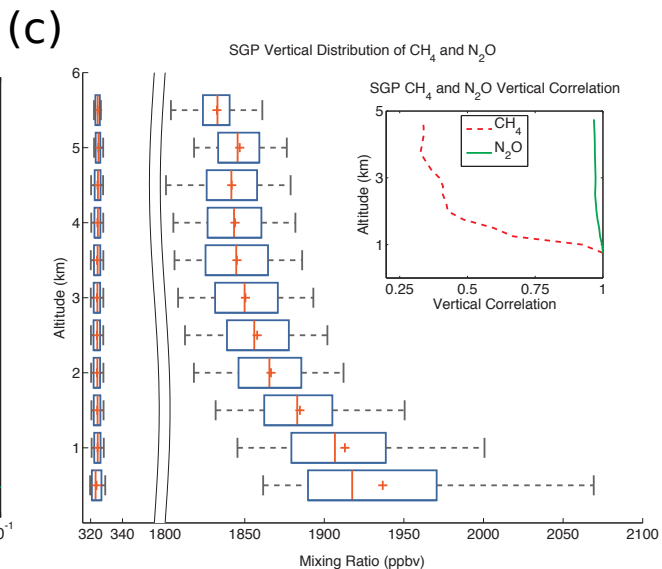
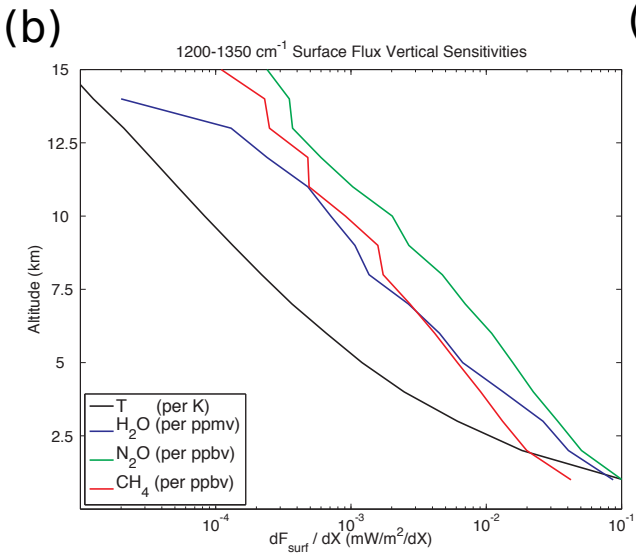
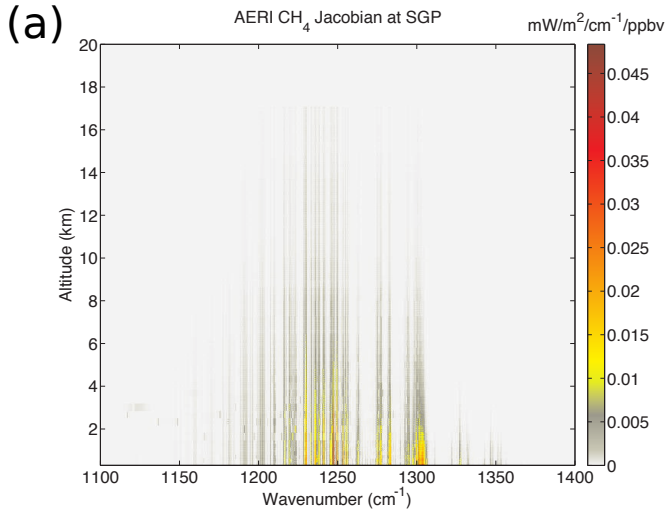
- 735 50. Clough, S.A., *et al.* Atmospheric radiative transfer modeling: a summary of the AER  
736 codes. *J. Quant. Spectrosc. Rad. Trans.* **91**, 233-244 (2005).
- 737 51. Rothman, L.S. *et al.* The HITRAN 2008 molecular spectroscopic database, *J. Quant.*  
738 *Spectrosc. Rad. Trans.* **110**, 533-572 (2009).
- 739 52. Alvarado, M.J., *et al.* Impacts of updated spectroscopy on thermal infrared retrievals of  
740 methane evaluated with HIPPO data. **8**, 965-985 (2015).
- 741 53. Li, J. Gaussian Quadrature and Its Application to Infrared Radiation. *J. Atmos. Sci.* **57**,  
742 753–765 (2000).
- 743 54. Turner, D.D., Knuteson, R.O., Revercomb, H.E., Lo, C. & Dedecker, R.G. Noise  
744 Reduction of Atmospheric Emitted Radiance Interferometer (AERI) Observations Using  
745 Principal Component Analysis. *J. Atmos. Oceanic Technol.* **23**, 1223-1238 (2006).
- 746 55. Wang, J., *et al.* Corrections of Humidity Measurement Errors from the Vaisala RS80  
747 Radiosonde – Application to TOGA COARE Data. *J. Atmos. Oceanic Technol.* **19**, 981-  
748 1002 (2002).
- 749 56. Turner, D.D., *et al.* Dry bias and variability in Vaisala radiosondes: The ARM  
750 experience. *J. Atmos. Oceanic Technol.* **20**, 117-132 (2003).
- 751 57. Weatherhead, E.C., *et al.* Factors affecting the detection of trends: Statistical  
752 considerations and applications to environmental data, *J. Geophys. Res.*, **103**, 17149-  
753 17161 (1998).
- 754 58. Liu, X., *et al.* OMI Ozone Profile and Tropospheric Ozone and Cross Evaluations with  
755 Chemical Transport Models, *AGU Meeting of the Americas*, A31A-22 (2013).
- 756 59. Kuhn, M. & Johnson. K. *Regression trees and rule-based models in Applied Predictive*  
757 *Modeling* (Springer, New York, 2013).

- 758 60. Shumway, R.H. & Stoffer., D.S. *Time Series Analysis and Its Applications*. (Springer,  
759 New York, 2000).
- 760 61. Ivosev, G., Burton, L. & Bonner, R. Dimensionality reduction and visualization in  
761 principal component analysis. *Anal. Chem.* **80**, 4933 (2008).
- 762 62. Frank, R.J., Davey, N. & Hunt, S.P. Time series prediction and neural networks. *Journal*  
763 *of Intelligent and Robotic Systems.* **31**, 91–103 (2001).
- 764 63. Casella, G. & Berger, R.L. *Statistical Inference Ch. 7.2.2* (Duxbury Press, Ithaca, NY,  
765 (2002).
- 766 64. Ravishanker, N. & Dey, D. *A First Course in Linear Model Theory* (Chapman and  
767 Hall/CRC, 2002).
- 768 65. Casella, G. & Berger, R.L. *Statistical Inference Ch. 10.4* (Duxbury Press, Ithaca, NY,  
769 (2002).
- 770 66. Gilks, W.R., Richardson, S. & Spiegelhalter, D.J. *Markov Chain Monte Carlo in Practice*  
771 (Chapman and Hall/CRC, 1995).
- 772 67. Kass, R. E. & Raftery, A.E. Bayes Factors. *J. Am. Stat. Assoc.* **90**, 773-795 (1995).
- 773 68. Bouwman, A.F., Boumans, L.J.M. & Batjes, N.H. Modeling global annual N<sub>2</sub>O and NO  
774 emissions from fertilized fields. *Global Biogeochem. Cy.* **16**, 1080 (2002).
- 775 69. Fulton, R.A., Breidenbach, J.P., Seo, D.J., Miller, D.A. & O'Bannon, T. The WSR-88D  
776 Rainfall Algorithm. *Wea. Forecasting.* **13**, 377–395 (1998).
- 777 70. Thoning, K.W., Tans, P. P. & Komhyr, W. D. Atmospheric carbon-dioxide at Mauna Loa  
778 observatory .2. analysis of the NOAA GMCC data, 1974-1985. *J. Geophys. Res.* **94**,  
779 8459-8565 (1989).

- 780 71. Mlawer, E.J., *et al.* The broadband heating rate profile (BBHRP) VAP. *Proc. 12th ARM*  
781 *Sci. Team Meet.* ARM-CONF-2002, US Department of Energy (2002).
- 782 72. Bruhwiler, L.M., *et al.* CarbonTracker-CH<sub>4</sub>: an assimilation system for estimating  
783 emissions of atmospheric methane. *Atmos. Chem. Phys.* **14**, 8269–8293 (2014).
- 784 73. McFarlane, S., T. Shippert, J. Mather. (2011). Radiatively Important Parameters Best  
785 Estimate (RIPBE): an ARM value-added product. DOE Tech. Rep. SC-ARM/TR-097 US  
786 Department of Energy.
- 787 74. Dlugokencky, E.J., Steele, L.P., Lang P.M. & Masarie, K.A. The growth rate and  
788 distribution of atmospheric methane. *J. Geophys. Res.* **99**, 17021-17043 (1994).
- 789 75. Knuteson, R.O., *et al.* Atmospheric Emitted Radiance Interferometer. Part II: Instrument  
790 Performance. *J. Atmos. Ocean. Technol.* **21**, 1777–1789 (2004).

# SGP CH<sub>4</sub> Flask Measurements Box-Whisker Plot







# SGP CH<sub>4</sub> Forcing

